Enhanced Recognition of Naval Ship HRRP Targets Using Improved Adaptive Threshold Wavelet Denoising

Zirong HONG [1,2], Qinfen LU [3], Guangqing BAO [3,4]

[1] Dept. of Electrical Engineering and Information Engineering, Lanzhou University of Technology, Lanzhou Gansu 730050, China
[2] School of Innovation and Entrepreneurship, Lanzhou Petrochemical University of Vocational Technology, Lanzhou Gansu 730060, China
[3] College of Electrical Engineering, Zhejiang University, Hangzhou Zhejiang310027, China
[4] School of Electronics and Information Engineering, Southwest Petroleum University, Chengdu Sichuan 610500, China

hzrsll@163.com, luqinfen@zju.edu.cn, baogq03@163.com

Submitted September 21, 2025 / Accepted November 13, 2025 / Online first January 9, 2026

Abstract. *To address the challenges of noise interference and low signal-to-noise ratio (SNR) in measured one-dimensional ship range profile data, which significantly affect target recognition, a new method is proposed. An improved adaptive threshold wavelet denoising (IATWD) method is introduced. Initially, the two critical parameters of wavelet denoising (WD)—namely, the threshold and threshold functions (TFs)—are optimized. For threshold optimization, a formula related to the number of decomposition levels, the noise standard deviations per level, and the signal length is developed. As decomposition levels change, an optimal threshold can be adaptively determined for each level. Regarding threshold function (TF) improvement, an enhanced TF is designed that flexibly adjusts based on the benefits of both soft and hard TFs. Subsequently, by analyzing the interactions between the variable factors, wavelet base functions, and decomposition levels, optimal parameters for this denoising method are selected. Finally, the efficacy of the denoising and its impact on recognition were validated using denoising evaluation metrics and a Support Vector Machine (SVM) for both simulated and empirical data. Experimental results with both data types demonstrate that the IATWD method significantly outperforms both traditional WD and comparative improved methods in terms of denoising effectiveness and recognition rates.*

Keywords

High resolution range profiles, classification recognition, adaptive threshold, improved threshold functions, wavelet denoising

1. Introduction

High Resolution Range Profiles (HRRP) represent the superposition of sub-echoes from target scattering points along the radar line of sight. These profiles encapsulate the rich structural features of the targets and hold considerable potential for applications in the field of ship recognition. However, when employing high-resolution unidimensional range profiles for empirical studies of ship target recognition [1–3], the experimental data inevitably includes disturbances such as sea clutter, rain and snow clutter, co-frequency interference, and internal noise [4], [5]. These disturbances reduce the SNR, blur the target information extracted from the range profiles, and severely impact the effectiveness of target recognition. Therefore, prior to conducting research on the classification and recognition of actual ship signals, it is essential to perform noise reduction on the unidimensional range profile data to enhance the recognition accuracy.

Among the various denoising methods available, wavelet transform (WT) is widely utilized due to its excellent multi-resolution characteristics. It retains the advantages of Fourier methods while providing the beneficial localization properties of the short-time Fourier transform, making it suitable for non-stationary signals. The ability of the WT to effectively handle transient changes in signals has led to its broad application in signal denoising and other areas [6], [7]. Although extensive research has been conducted on wavelet denoising (WD) in various fields such as biomedical imaging [8], microscopy [9], bearing fault diagnosis [10–12], and precision agriculture [13], literature on WD in the field of ship recognition is relatively scarce. In fact, the effective information in HRRP ship signals typically concentrates in a few scattering centers, characterized by their non-stationarity and sparsity, making them particularly suitable for wavelet-based denoising.

The parameters involved in WD include the wavelet base, decomposition levels, thresholds, and TFs, where the selection and design of thresholds and TFs are critical factors influencing the denoising outcome. Existing research predominantly focuses on these key parameters. Zheng et al. [14] proposed a denoising algorithm based on

DOI: 10.13164/re.2026.0041

an adaptive threshold recursive cyclic rotation using the Shearlet transform. Liu et al. [15] introduced a method for attenuating seismic stochastic noise, leveraging the scale and directional characteristics of the Shear wave transform through an adaptive threshold. Li et al. [16] modified the thresholding approach based on the VisuShrink fixed threshold method and introduced improved TFs. Lu et al. [17] developed an improved TFs associated with decomposition levels for denoising vibration signals in ore supply pipeline systems. Wu et al. [18] constructed a TF that is continuous and differentiable at the threshold point to address the reconstruction bias and excessive denoising flaws inherent in traditional TFs. However, these methods, while straightforward and easy to implement, do not account for the statistical properties of the signal components post-decomposition, and their improved TFs lack flexibility, leading to poor adaptivity and significant bias, thus rendering the denoising effect suboptimal.

To achieve better denoising outcomes and accurately identify naval ships, this study builds upon the aforementioned studies by utilizing wavelet coefficients from each level of WT as parameters for threshold calculation. It proposes a novel method for adaptive threshold computation and designs an improved TF with a variable factor for flexible adjustment. Both simulation and real data validate the better denoising performance and higher recognition rates of the proposed improved adaptive threshold wavelet denoising (IATWD) method. This study is organized as follows: Section 2 introduces the fundamental principles of WD, including WT, decomposition, and reconstruction. Section 3 improves upon the VisuShrink threshold and designs an adaptive threshold formula. Based on the merits and demerits of soft and hard TFs, it proposes an improved wavelet threshold denoising function. Section 4 validates the IATWD using simulation data, comparing variable factors, wavelet bases, and decomposition levels to determine optimal parameters. The denoising effect of the method is validated through comparisons involving various thresholds and TFs, and by classifying ship targets using a Support Vector Machine (SVM) to assess the method's recognition capabilities. Section 5 discusses the limitations of using the SNR and root mean square error (RMSE) as evaluation metrics, due to the absence of original, pure signals in actual data. Instead, it employs energy ratio and Local Peak Signal-to-Noise Ratio (LPSNR) to validate the denoising efficacy of the IATWD method and to perform recognition verification. Section 6 provides a summary.

2. Fundamental Principles of WD

The process of WD involves the following steps: Initially, an appropriate wavelet base and decomposition levels are selected to decompose the signal into a collection of wavelet coefficients. Subsequently, suitable thresholds and TFs are chosen to denoise the decomposed wavelet coefficients, resulting in new wavelet coefficients. Finally, these new wavelet coefficients are reconstructed to obtain the desired signal.

2.1 Wavelet Transform (WT)

1. Continuous Wavelet Transform (CWT)

The function space for the WT is generally $L^2(R)$, which represents the collection of functions that are square-integrable on the real number domain R. This is mathematically represented as:

$$\psi(t) = L^2(R). \tag{1}$$

A function $\psi(t) \in L^2(R)$ is termed an energy-limited signal. If $\psi(t)$ also satisfies the admissibility condition following its Fourier transform $\psi(\omega)$,

$$\int_R \frac{|\psi(\omega)|^2}{|\omega|} \mathrm{d}t < +\infty \tag{2}$$

it is defined as a mother wavelet [19]. By scaling and translating the mother wavelet, a family of wavelets, $\psi_{a,b}(t) = |a|^{\frac{-1}{2}} \psi(\frac{x-b}{a})$, is generated. In this context, a serves as the scaling factor where $a \in R^+$, while $b \in R$ functions as the translation factor.

The formula for the CWT [20] of a function $f(t)$ using the base wavelet ψ is given by [21]:

$$(W_\psi f)(a,b) = \langle f, \psi_{a,b} \rangle = |a|^{-\frac{1}{2}} \int_{-\infty}^{+\infty} f(t) \overline{\psi\left(\frac{t-b}{a}\right)} \mathrm{d}t \tag{3}$$

where $\overline{\psi(\frac{t-b}{a})}$ denotes the complex conjugate of $\psi(\frac{t-b}{a})$. The WT converts a one-dimensional signal into a two-dimensional function, enabling a more thorough examination of the signal's time-frequency properties. The inverse transformation:

$$f(t) = \frac{1}{C_\psi} \int_{-\infty}^{+\infty} \int_{-\infty}^{+\infty} \left[(W_\psi f)(a,b)\right] \psi_{a,b}(x) \frac{\mathrm{d}a\,\mathrm{d}b}{a^2} \tag{4}$$

is the wavelet inverse transform for the function $f(t)$ with respect to the base wavelet ψ, which reconstructs the original signal from the wavelet-transformed data.

2. Discrete Wavelet Transform (DWT)

The CWT involves continuous scaling and translation factors, necessitating the computation of continuous integrals, which can be inconvenient for practical applications. In practice, the DWT [22] is often employed. The DWT discretizes the scaling factor a and the translation factor b of the CWT. Common selections for these parameters are $a = a_0^m$, $b = nb_0 a_0^m$ where $m,n \in Z$, resulting in a discrete set of wavelet functions:

$$\psi_{m,n}(t) = |a_0|^{-\frac{m}{2}} \psi(a_0^{-m} t - nb_0), m, n \in Z. \tag{5}$$

In this scenario, the wavelet functions are discrete, and the corresponding DWT is described as:

$$\left(W_\psi f\right)(a,b)=\left\langle f,\psi_{a,b}\right\rangle=|a|^{-\frac{m}{2}}\int_{-\infty}^{+\infty} f(t)\overline{\psi\left(a_0^{-m}t-nb_0\right)}\mathrm{d}t. \quad (6)$$

Specifically, setting $a_0 = 2$, $b_0 = 1$yields the dyadic wavelet:

$$\psi_{m,n}(t)=2^{-\frac{m}{2}}\psi(2^{-m}t-n), m,n\in Z. \quad (7)$$

2.2 Wavelet Decomposition and Reconstruction

In the context of DWT, grounded in the theory of orthogonal multiresolution analysis, the linear function spaces $\{V_j : j \in Z\}$ can be decomposed into a direct sum of V_{j-1} and its orthogonal projection within V_j, denoted as W_{j-1}. This is formally represented as $V_j = V_{j-1} \oplus W_{j-1}$, where j indexes the resolution level. Additionally, it holds that $V_{j-1} \perp W_{j-1}$, $j \in Z$. Consequently, any signal $x(t)$ represented on V_j can be expressed using the basis functions $\phi_{j-i,k}(t)$ for V_{j-1} and $\psi_{j-i,k}(t)$ for W_{j-1}, as shown in [23]:

$$\begin{aligned} x(t)&=\sum_k c_{j,k}\phi_{j,k}(t)\\ &=\sum_k c_{j-1,k}\phi_{j-1,k}(t)+\sum_k d_{j-1,k}\psi_{j-1,k}(t)\end{aligned}. \quad (8)$$

Here, $k \in Z$, where $\phi_{j-1,k}(t)$ represents the scaling function, and $\psi_{j-1,k}(t)$ denotes the wavelet function; $c_{j-1,k}$ are the scaling coefficients, and $d_{j-1,k}$ are the wavelet coefficients.

This decomposition can be implemented via a specific set of filters. When the wavelet and scaling functions are orthogonal in space, the scaling coefficients $c_{j-1,k}$ and wavelet coefficients $d_{j-1,k}$ can be calculated using the inner product formula:

$$\begin{aligned} c_{j-1,k}&=\left\langle x(t),\phi_{j-1,k}(t)\right\rangle\\ &=\left\langle\sum_n c_{j,n}\phi_{j,n}(t),\phi_{j-1,k}(t)\right\rangle\\ &=\sum_n c_{j,n}\left\langle\phi_{j,n}(t),\phi_{j-1,k}(t)\right\rangle\\ &=\sum_n h(n-2k)c_{j,n}\end{aligned}, \quad (9)$$

$$\begin{aligned} d_{j-1,k}&=\left\langle x(t),\psi_{j-1,k}(t)\right\rangle\\ &=\left\langle\sum_n c_{j,n}\phi_{j,n}(t),\psi_{j-1,k}(t)\right\rangle\\ &=\sum_n c_{j,n}\left\langle\phi_{j,n}(t),\psi_{j-1,k}(t)\right\rangle\\ &=\sum_n g(n-2k)c_{j,n}\end{aligned}. \quad (10)$$

Here, $n \in Z$. The functions $h(n - 2k)$ and $g(n - 2k)$ [24] can be considered as low-pass and high-pass filters, respectively. The principle of wavelet decomposition and reconstruction [25] involves passing the signal through a pair of high-pass and low-pass filters to obtain a set of wavelet and scaling coefficients. This process is continued using further pairs of filters to achieve subsequent sets of coefficients until the desired number of decomposition levels is reached, effectively accomplishing the wavelet decomposition of the signal. Similarly, the wavelet reconstruction algorithm can be viewed as the inverse process of the decomposition algorithm. The process flowcharts for wavelet decomposition and reconstruction are illustrated in Figs. 1 and 2.

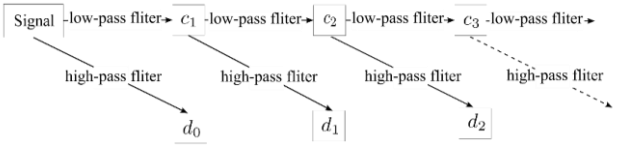

Fig. 1. Wavelet decomposition flowchart.

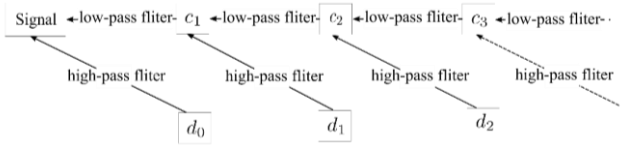

Fig. 2. Wavelet decomposition flowchart.

3. Determination of Adaptive Threshold and Improved TF

3.1 Determination of Adaptive Threshold

The selection of thresholds is a critical component in the wavelet threshold denoising process. A key criterion for this selection is minimizing the discrepancy between the coefficients $d_{j,k}$ (the wavelet coefficient of original signal) and $\hat{d}_{j,k}$ (the wavelet coefficient after noise reduction) and the original signal to avoid significant deviations from the original. Common threshold selection methods include the VisuShrink threshold, the Minimax criterion threshold, and Rigrsure threshold [26–28]. However, the noise coefficients in wavelet decomposition decrease with increasing levels of decomposition, limiting the effectiveness of a fixed threshold. Consequently, numerous scholars have built upon the VisuShrink threshold method to propose various formulas for adaptive thresholds, as illustrated below:

(1) VisuShrink threshold

$$T=\sigma\sqrt{2\ln n} \quad (11)$$

(2) Adaptive threshold [17]

$$T_j=\frac{\sigma\sqrt{2\ln n}}{\ln(j+1)} \quad (12)$$

(3) Adaptive threshold [16]

$$T_j=\frac{\sigma\sqrt{2\log_2 n_j}}{\ln(j+1)} \quad (13)$$

These formulas incorporate parameters such as the signal length n, j denotes the decomposition levels, n_j indicates the length of the detail coefficients at the j-th level, and σ represents the standard deviation (std) of the noise signal. The standard deviation (std) of the noise is estimated using the median absolute deviation (MAD) [29], defined as σ = MAD/0.6745. Here, MAD = median($|d_{1,k}|$).

The aforementioned improved TFs primarily consider the effects of decomposition scale and signal length on the threshold values. Building on this foundation, this study further refines the approach by not only considering the influence of decomposition scale but also the std of the noise at each level and the signal length. As the number of decomposition levels changes, each level adaptively derives the optimal threshold, demonstrated in the following equation (14):

$$T_j = \gamma^j \sigma_j \sqrt{2\ln n_j} \,. \tag{14}$$

Here, n_j indicates the length of the detail coefficients at the j-th level, j denotes the decomposition levels, σ_j represents the std at the j-th level, where σ_j = median($|d_{j,k}|$)/0.6745, γ represents the scale attenuation factor, which controls the attenuation degree of thresholds among different wavelet scales.

3.2 Improved Wavelet TF

In the domain of wavelet threshold denoising, the selection of appropriate TF is a crucial factor determining the ultimate effectiveness of noise reduction. Commonly employed wavelet threshold selection functions include hard thresholding, soft thresholding, and garrote thresholding. Although these three methodologies ensure a certain level of noise suppression, their inherent limitations suggest significant room for improvement in denoising performance.

Li et al. [16] and Lu et al. [17] have enhanced the TFs by embedding an exponential function into the thresholding process. This modification aims to accelerate computational efficiency. However, challenges persist due to signal compression and bias introduced by soft thresholding, resulting in the direct discarding of wavelet coefficients beneath the threshold, thereby constraining the preservation of low-frequency components. The expressions for the TFs presented by Li et al. [16] and Lu et al. [17] are illustrated below:

$$\hat{d}_{j,k} = \begin{cases} d_{j,k} - \dfrac{\operatorname{sgn}\left(d_{j,k}\right)}{\mathrm{e}^{30\left(\sqrt{|d_{j,k}|/T}-1\right)}}, & |d_{j,k}| \ge T \\ 0, & |d_{j,k}| < T \end{cases}, \tag{15}$$

$$\hat{d}_{j,k} = \begin{cases} \operatorname{sgn}(d_{j,k})\left(d_{j,k} - \dfrac{T}{(|d_{j,k}|-T)^j + 1}\right), & |d_{j,k}| \ge T \\ 0, & |d_{j,k}| < T \end{cases}. \tag{16}$$

Furthermore, Wu et al. [18], utilizing an unbiased likelihood estimation (Rigrsure threshold), proposed a moderately smooth TFs intended to combine the characteristics of both soft and hard thresholding. Although this method benefits from the merits of both functions, it exhibits certain limitations in terms of flexibility during signal adjustment. The expression for their TFs is presented below:

$$\hat{d}_{j,k} = \begin{cases} d_{j,k} - \dfrac{T^2}{3d_{j,k}} - \dfrac{\operatorname{sgn}\left(d_{j,k}\right)}{3\mathrm{e}^{|d_{j,k}|-T}}, & |d_{j,k}| \ge T \\ \dfrac{d_{j,k}}{3}\mathrm{e}^{|d_{j,k}|-T}, & |d_{j,k}| < T \end{cases}. \tag{17}$$

Given these considerations, an ideal TF should maintain continuity, avoiding discontinuities at the threshold; it should approximate the original wavelet coefficients as closely as possible to minimize constant bias; and it should preserve and enhance the advantages of traditional TFs while offering flexibility. Therefore, this study integrates the advantages of both soft and hard TFs by incorporating an exponential function into the TF. An improved TF that is continuous at the threshold points T and kT and has an adjustable factor is constructed, as shown in (18):

$$\hat{d}_{j,k} = \begin{cases} \operatorname{sgn}\left(d_{j,k}\right)\left(|d_{j,k}| - (1-a(1-\mathrm{e}^{-1})kT\,\mathrm{e}^{\frac{-1}{(1-a)}\left(\frac{|d_{j,k}|-kT}{kT}\right)^2}\right), & |d_{j,k}| \ge kT \\ \operatorname{sgn}\left(d_{j,k}\right)a|d_{j,k}|\left(1-\mathrm{e}^{\left(\frac{|d_{j,k}|-T}{kT-T}\right)^2}\right), & T \le |d_{j,k}| < kT \\ 0, & |d_{j,k}| < T \end{cases} \tag{18}$$

In this improved TF, k is the threshold adjustment factor, the value range is $k > 1$, and the wavelet coefficients larger than the threshold are segmented to determine the shrinkage degree of the coefficients in different intervals; a is a variable factor, and its value range is [0, 1). The flexibility of these functions can be adjusted by modifying the value of a, thereby tailoring the outcome to specific applications. It can be seen that the variable factors $a \in [0, 1)$, $\hat{d}_{j,k}$ are between the coefficients calculated by the soft and hard TFs.

Initially, the parity of the improved TF is examined:

For $0 \le a < 1$, $\hat{d}_{j,k}(-d_{j,k}) = -\hat{d}_{j,k}(d_{j,k})$, indicating that the TFs are odd functions.

Next, the continuity of the improved TF is assessed:

When $d_{j,k} \to kT^{+}$,

$$\begin{aligned}\lim_{d_{j,k}\to kT^{+}} \hat{d}_{j,k} &= \lim_{d_{j,k}\to kT^{+}} \left|d_{j,k}\right| - kT\,\mathrm{e}^{\frac{-1}{(1-a)}\left(\frac{|d_{j,k}|-kT}{kT}\right)^2} \\ &\quad + a(1-\mathrm{e}^{-1})kT\,\mathrm{e}^{\frac{-1}{(1-a)}\left(\frac{|d_{j,k}|-kT}{kT}\right)^2} \\ &= \lim_{d_{j,k}\to kT^{+}} \left|d_{j,k}\right| - kT\,\mathrm{e}^{-\infty} + a(1-\mathrm{e}^{-1})kT\,\mathrm{e}^{-\infty} \\ &= \lim_{d_{j,k}\to kT^{+}} k - kT + a(1-\mathrm{e}^{-1})kT \\ &= akT(1-\mathrm{e}^{-1}).\end{aligned} \tag{19}$$

When $d_{j,k} \to kT^{-}$,

$$\begin{aligned}\lim_{d_{j,k}\to kT^{-}} \hat{d}_{j,k} &= \lim_{d_{j,k}\to kT^{-}} a\left|d_{j,k}\right|\left(1-\mathrm{e}^{-\left(\frac{|d_{j,k}|-T}{kT-T}\right)^2}\right) \\ &= \lim_{d_{j,k}\to kT^{-}} a\left|d_{j,k}\right|(1-\mathrm{e}^{-1}) \\ &= akT(1-\mathrm{e}^{-1}).\end{aligned} \tag{20}$$

When $d_{j,k} \to T^{+}$,

$$\begin{aligned}\lim_{d_{j,k}\to T^{+}} \hat{d}_{j,k} &= \lim_{d_{j,k}\to T^{+}} a\left|d_{j,k}\right|\left(1-\mathrm{e}^{-\left(\frac{|d_{j,k}|-T}{kT-T}\right)^2}\right) \\ &= \lim_{d_{j,k}\to kT^{+}} a\left|d_{j,k}\right|(1-\mathrm{e}^{0}) \\ &= 0.\end{aligned} \tag{21}$$

When $d_{j,k} \to T^{-}$,

$$\lim_{d_{j,k}\to T^{-}} \hat{d}_{j,k} = 0. \tag{22}$$

From the above, it is evident that $\lim_{d_{j,k}\to kT^{+}} \hat{d}_{j,k} = \lim_{d_{j,k}\to kT^{-}} \hat{d}_{j,k} = akT(1-\mathrm{e}^{-1})$, $\lim_{d_{j,k}\to T^{+}} \hat{d}_{j,k} = \lim_{d_{j,k}\to T^{-}} \hat{d}_{j,k} = 0$, confirming that the improved TF are continuous at threshold T and kT, and similarly at threshold $-T$ and $-kT$. Therefore, the improved TF is continuous at both $\pm T$ and $\pm kT$, which mitigates the signal oscillations inherent in hard TF.

The asymptotic behavior of the improved TF is then verified:

When $|d_{j,k}| \to \infty$,

$$\begin{aligned}\lim_{|d_{j,k}|\to\infty} \frac{\hat{d}_{j,k}}{d_{j,k}} &= \lim_{|d_{j,k}|\to\infty} \frac{\mathrm{sgn}(d_{j,k})\left|d_{j,k}\right|}{d_{j,k}} \\ &\quad - \frac{(1-a(1-\mathrm{e}^{-1}))kT\,\mathrm{e}^{\frac{-1}{(1-a)}\left(\frac{|d_{j,k}|-kT}{kT}\right)^2}}{d_{j,k}} \\ &= \lim_{|d_{j,k}|\to\infty} 1 - \frac{(1-a(1-\mathrm{e}^{-1}))kT\times 0}{d_{j,k}} \\ &= 1,\end{aligned} \tag{23}$$

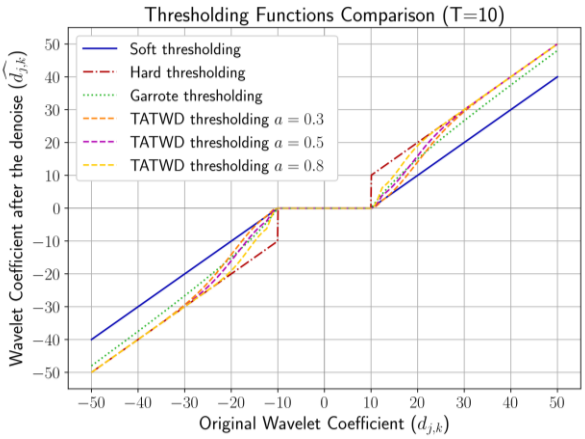

Fig. 3. Comparison of improved TF with soft, hard, and garrote TFs.

$$\begin{aligned}\lim_{|d_{j,k}|\to\infty} \hat{d}_{j,k} - d_{j,k} &= \lim_{|d_{j,k}|\to\infty} \mathrm{sgn}(d_{j,k})\left|d_{j,k}\right| - d_{j,k} \\ &\quad - \mathrm{sgn}(d_{j,k})(1-a(1-\mathrm{e}^{-1}))kT\,\mathrm{e}^{\frac{-1}{(1-a)}\left(\frac{|d_{j,k}|-kT}{kT}\right)^2} \\ &= \lim_{|d_{j,k}|\to\infty} -\mathrm{sgn}(d_{j,k})(1-a(1-\mathrm{e}^{-1}))kT\times 0 \\ &= 0.\end{aligned} \tag{24}$$

It can be determined that the asymptote of $\hat{d}_{j,k}$ is $d_{j,k}$ and as $|d_{j,k}| \to \infty$, the transformed wavelet coefficients $\hat{d}_{j,k}$ gradually converge to the original coefficients, eliminating the constant bias between them. Thus, the reconstructed signal does not suffer from degradation, and the denoising effect is further enhanced. Setting $k = 1.24$, $T = 10$, the comparison of the improved TF with traditional soft, hard, and garrote TFs is illustrated in Fig. 3.

The graph demonstrates continuity at thresholds T and kT, and shows that as $|d_{j,k}| \to \infty$, $\hat{d}_{j,k}$ gradually converges to $d_{j,k}$, without any constant bias.

4. Simulation Data Verification for IATWD Method Denoising

4.1 Threshold Introduction to Simulation Data

The simulation data employed in this study includes models of four types of naval ships, constructed using 3dsMAX software. The models include a Cruise Ship (CST), a Tugboat (TUO), the "Burke-class destroyer USS Murphy" DDG112, and the "Enterprise-class aircraft carrier" CVN-65. HRRP data was generated using electromagnetic computation software FEKO [30], with the following parameters: radar central frequency of 12 GHz, bandwidth of 150 MHz. Data was generated for a full azimuthal range of 0–360 degrees at 1-degree intervals, with 400 range cells and a resolution of 1 meter. The parameters of the simulated naval ships are shown in Tab. 1.

Target	Length	Width	Height
CST	131 m	20 m	22 m
TUO	102.8 m	17.4 m	38.5 m
DDG112	153.6 m	19.2 m	52.6 m
CVN-65	342.3 m	73.9 m	64.5 m

Tab. 1. Target dimension parameters.

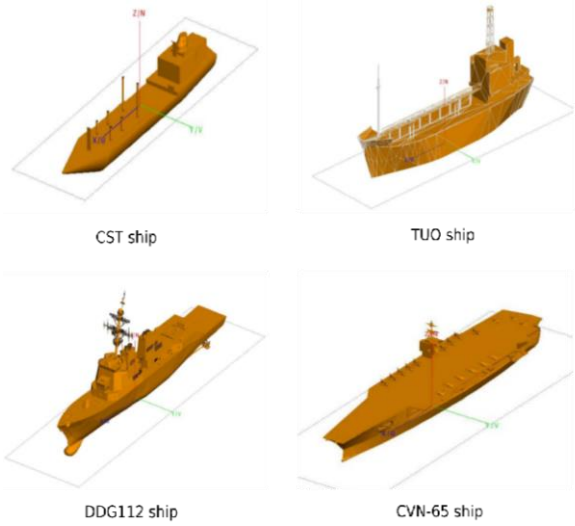

Fig. 4. Schematic of naval ship models for simulation.

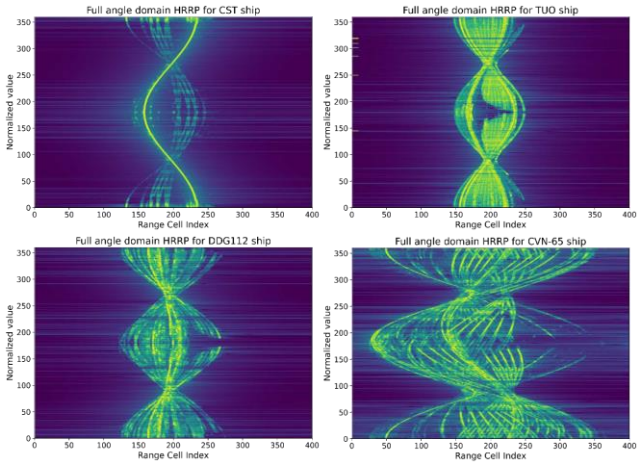

Fig. 5. Full azimuthal domain HRRP of ship targets.

A schematic of the simulation models for the four classes of ships is shown in Fig. 4. The full azimuthal domain HRRP display of the ship targets is presented in Fig. 5.

4.2 Validation of IATWD Method Denoising Effectiveness

HRRP is the amplitude value of the radar target scattering echo, and the amplitude is non-negative in the physical sense. By adding Gaussian complex noise with complex domain plus noise and an independent Gaussian distribution of real and imaginary parts [31], the physical process and statistical characteristics of HRRP noise can be restored, which is a reasonable choice for simulating HRRP noise. However, the added Gaussian complex noise generates an 'asymmetric distribution offset' (Direct Current (DC) Bias Characteristic) due to the physical amplitude constraint, which makes the statistical mean of the overall noise deviate from 0 and greater than 0. The core logic of wavelet denoising is to separate the signal and noise through 'high frequency threshold filtering', which cannot effectively solve the problem of DC bias characteristics caused by adding complex noise, and reduces the denoising quality of the data. The DC bias characteristics of the denoised data are corrected. The baseline of the DC bias of the complex Gaussian noise is estimated by one-dimensional minimum filtering. The threshold is used to distinguish the peak and non-peak regions of the target. The non-peak region is subtracted from the baseline optimized by linear interpolation, and the peak region is retained to eliminate the DC bias and retain the effective signal of the target.

$$\hat{s}(n)=\begin{cases} y(n), & y(n)\geq \mu+\lambda\sigma \\ \max\{y(n)-b(n),0\}, & y(n)<\mu+\lambda\sigma \end{cases}. \quad (25)$$

In the formula, $y(n)$ represents the denoised signal, $\hat{s}(n)$ denotes the corrected signal after denoising treatment, μ is the mean value of the denoised signal, σ is the std of the denoised signal, σ = MAD/0.6745, λ is the threshold factor, distinguishing the target peak and non-peak regions, $b(n) = \min\{y(n-t),\ldots, y(n+t)\}$ is the baseline estimate of the DC bias of the complex Gaussian noise, which is preliminarily estimated by the one-dimensional minimum filter with a window size of $2t + 1$, and max{ ,0} represents the non-negative truncation of the non-peak region corrected result.

In this study, simulation data from four types of naval ships were used as original signals. To each, add a 5 dB of complex Gaussian white noise, and the corrected data after noise reduction were used for comparative experiments. The objective was to identify the optimal denoising scheme by experimenting with various wavelet bases, levels of wavelet decomposition, TFs, and threshold types. By comparing the waveform distortion under various conditions, as well as the SNR and RMSE of the noise reduction corrected signal, it was found that the noise reduction effect of IATWD was relatively good when parameters k = 1.24, γ = 0.95, t = 0.7, and λ = 0.5 were used. Whether for simulation data or measured data, these parameters were selected to verify the noise reduction.

The performance of the denoising algorithm was quantitatively assessed using the SNR and the RMSE as metrics [16]. Higher SNR and lower RMSE indicate a smaller discrepancy between the denoised and original signals, thus signifying better denoising effectiveness.

The formula for SNR is:

$$\mathrm{SNR}=10\log_{10}\left(\frac{\sum x^2(n)}{\sum\left[x(n)-\hat{s}(n)\right]^2}\right). \quad (26)$$

The formula for RMSE is:

$$\mathrm{RMSE} = \sqrt{\frac{\sum [x(n) - \hat{s}(n)]^2}{N}} . \tag{27}$$

In (26) and (27), $x(n)$ represents the original signal, and $\hat{s}(n)$ denotes the corrected signal after denoising treatment.

Taking the signal from the naval ship DDG112 as an example, denoising was conducted using different TFs and optimized thresholds. The variable factor a was first determined; then, keeping other parameters constant, the IATWD method was applied to all sample signals of DDG112 using various values of a, with the results displayed in Tab. 2. The results indicated that an a value of 0.8 yielded the highest average SNR and the lowest average RMSE for the denoised signals. Therefore, the adjustment factor a in the IATWD was set to 0.8.

To avoid distortion at the edges of signals and abrupt changes during multi-scale decomposition and reconstruction, the wavelet base should be chosen for its good regularity and symmetrical or nearly symmetrical biorthogonal properties. Accordingly, five wavelet bases of coif4, db2, db7, sym4 and sym8 in the three categories wavelet bases—sym, db, and coif [32], characterized by near-symmetry, minimal vanishing moments, and regularity—were selected. Table 3 illustrates the denoising effects of different wavelet bases on noisy signals, revealing that the db2 wavelet base achieved the highest average SNR and the smallest average RMSE post-denoising. Table 4 shows that when the decomposition levels were set to 5, the best denoising performance was obtained. Therefore, the db2 wavelet base and 5 decomposition levels were selected as parameters for subsequent signal processing tasks.

To ascertain the effectiveness of the proposed IATWD denoising method, this study compares the improved TFs developed herein with conventional soft, hard, and garrote thresholding techniques, as well as the denoising approaches detailed in the references [16–18]. The evaluations employed a db2 wavelet base, with a decomposition level of 5 and a variable factor of 0.8. The outcomes of these assessments are depicted in Tab. 5.

Table 5 presents the average SNR and average RMSE of all samples of the naval ship DDG112 processed by different denoising methods, while Figure 6 shows a comparison of amplitude values of a specific sample of the naval ship DDG112 obtained via different denoising methods. It can be seen from Tab. 5 that, compared with other denoising methods, the IATWD method proposed in this paper achieves the highest SNR values and the lowest RMSE values. As observed from Fig. 6, the hard (visushrink) method exhibits the pseudo-Gibbs phenomenon and has residual noise in the peak region. The soft (visushrink) method demonstrates better smoothness but causes excessive smoothing, leading to more loss of effective information in the denoised signal. The garrote (visushrink) applies a larger shrinkage ratio to weak scattering points, resulting in over-smoothing of these points. The denoising method of the reference [16] leaves a large amount of residual noise. The method of the reference [17] damages the detailed features of the signal. The method of the reference [18] causes severe damage to signal details and also retains a significant amount of residual noise. In contrast, the IATWD method not only reduces noise more effectively but also better preserves the signal's detailed characteristics. The results indicate that for the naval ship DDG112, the IATWD method offers the best noise reduction performance.

To conduct a comprehensive analysis of the denoising efficacy of the IATWD method, identical parameters were applied to naval ships CST, TUO, and CVN-65: a db2 wavelet base, five decomposition levels, and a variable factor of $a = 0.8$. The resulting SNR and RMSE from these evaluations are illustrated in Tab. 6. Table 6 demonstrates that, similar to the DDG112, the IATWD method achieves the highest SNR values and the lowest RMSE values across the different ships, indicating its broad adaptability as a denoising method.

In the study presented here, denoising experiments were conducted on simulated signals from four types of naval ships. The IATWD method designed in this study, employing identical parameters, was compared with conventional soft, hard and garrote TFs, as well as denoising methods outlined in the references [16–18]. The IATWD method demonstrated the highest SNR and the lowest RMSE, indicating its better denoising performance. In subsequent experiments involving both simulation and actual data for ship recognition, denoising was performed using the db2 wavelet base at a decomposition level of five, with a variable factor a set at 0.8.

a	**0.1**	**0.5**	**0.7**	**0.8**	**0.9**	**0.95**
SNR	13.84	14.50	14.84	15.13	14.87	14.70
RMSE	0.196	0.186	0.183	0.180	0.183	0.185

Tab. 2. Impact of different variable factor on the denoising of ship DDG112.

Wavelet base	**Coif4**	**db2**	**db7**	**sym4**	**sym8**
SNR	14.39	15.13	14.18	14.71	14.51
RMSE	0.195	0.180	0.189	0.185	0.192

Tab. 3. SNR and RMSE under different wavelet base treatments for DDG112.

Decomposition level	**Two-level**	**Three-level**	**Four-level**	**Five-level**	**Six-level**
SNR	13.03	14.31	14.67	15.13	14.82
RMSE	0.228	0.194	0.185	0.180	0.183

Tab. 4. SNR and RMSE at different decomposition levels of db2 for DDG112.

Denoising methods	Soft (visushrink)	Hard (visushrink)	Garrote (visushrink)	IATWD	Reference [16]	Reference [17]	Reference [18]
SNR	11.28	14.43	13.54	**15.13**	12.82	13.854	10.71
RMSE	0.279	0.191	0.206	**0.180**	0.261	0.237	0.392

Tab. 5. SNR and RMSE for various denoising methods applied to ship DDG112.

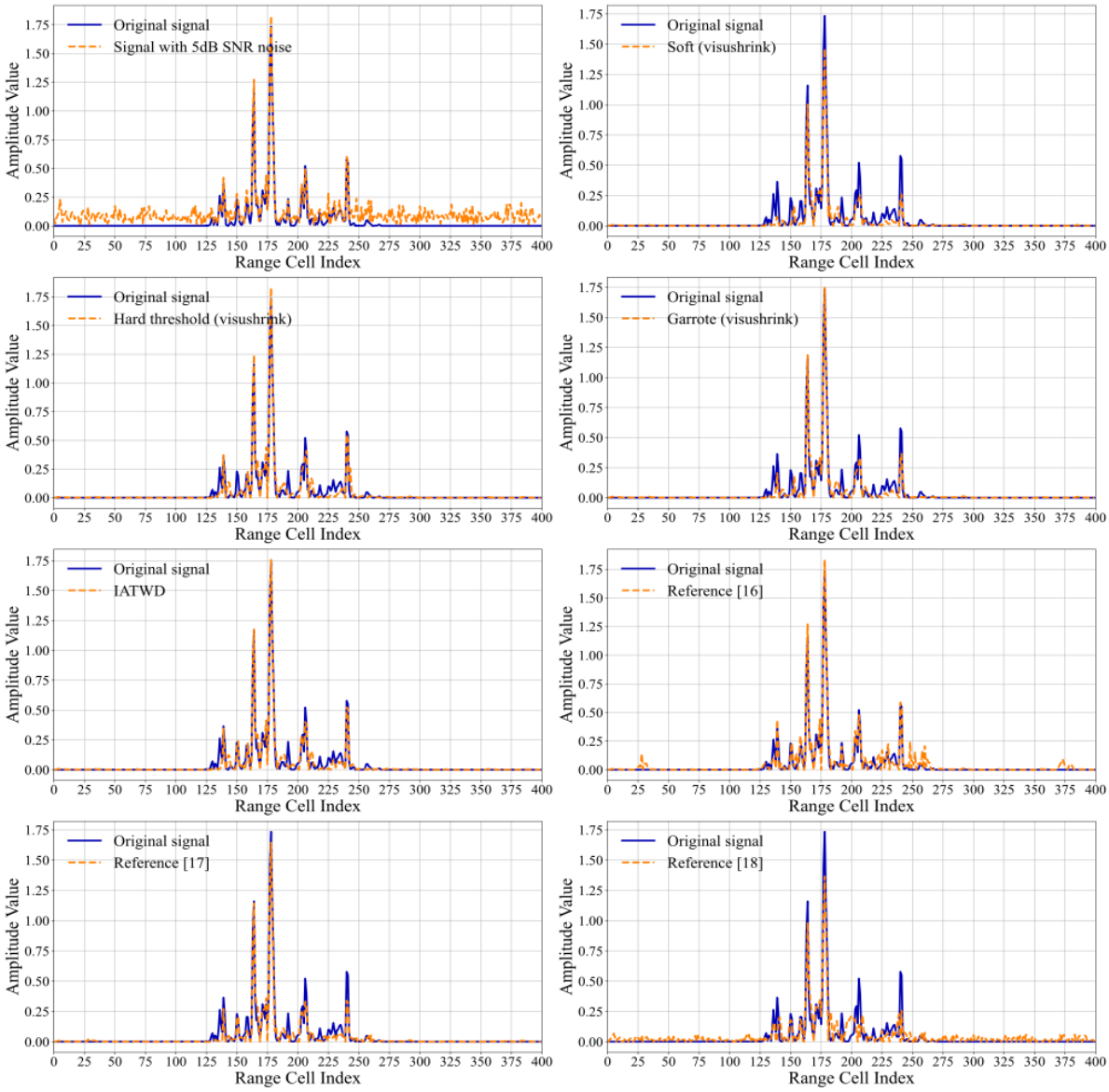

Fig. 6. Comparison of different denoising methods for a sample from naval ship DDG112.

Denoising methods	CST		TUO		CVN-65	
	SNR	RMSE	SNR	RMSE	SNR	RMSE
Soft (visushrink)	14.18	0.227	10.24	0.213	7.73	0.200
Hard (visushrink)	19.84	0.118	13.15	0.145	10.77	0.136
Garrote (visushrink)	18.51	0.137	12.34	0.158	9.543	0.158
IATWD	**20.79**	**0.106**	**14.62**	**0.126**	**11.72**	**0.124**
Reference [16]	14.19	0.236	12.31	0.159	11.28	0.129
Reference [17]	18.71	0.132	11.92	0.177	10.20	0.142
Reference [18]	12.81	0.277	8.225	0.264	7.43	0.205

Tab. 6. SNR and RMSE for various denoising methods applied to three ships.

4.3 Validation of the IATWD Method for Recognition Performance

To validate the recognition performance of the IATWD denoising method, denoised data were subjected to ship recognition analysis using the SVM. The kernel function for the SVM was the Radial Basis Function (RBF), and the parameters for the RBF and penalty factor were selected through cross-validation.

The dataset consisted of 1,440 multi-angle, HRRP observations from four different classes of ships, with 360 observations per class. For testing recognition, a random set of 72 observations from each class was selected, leaving the remainder for training. The evaluation metrics used were Accuracy, Precision, and Recall. The experiment was repeated ten times, with the average recognition rates depicted in Tab. 7, and a confusion matrix from one of the experiments shown in Fig. 7.

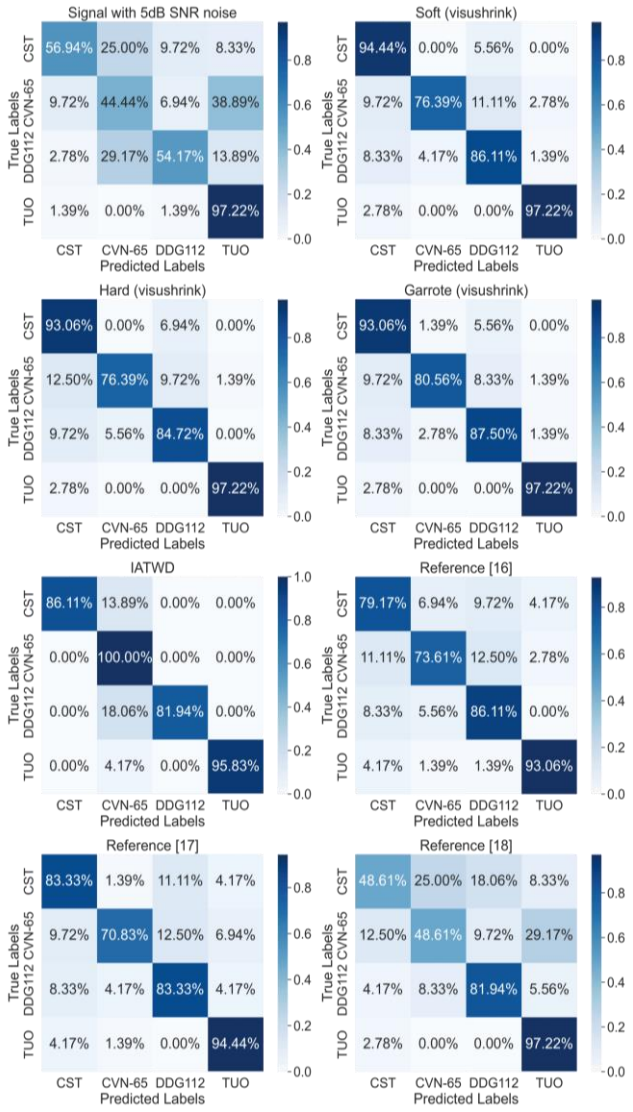

Fig. 7. Confusion matrix from one experiment for the recognition of four classes of simulated ships.

Different signal	Average Accuracy	Average Precision	Average Recall
Noisy signal	85.68%	72.63%	71.35%
Soft (visushrink)	94.41%	89.79%	88.82%
Hard (visushrink)	94.17%	89.46%	88.33%
Garrote (visushrink)	94.51%	90.05%	89.03%
IATWD	**95.19%**	**92.38%**	**90.38%**
Reference [16]	91.72%	84.26%	83.44%
Reference [17]	92.97%	86.58%	85.94%
Reference [18]	88.19%	76.55%	76.39%

Tab. 7. Average recognition rates (%) for different signals.

As indicated in Tab. 7, compared with other denoising methods, the IATWD method proposed in this paper achieves the highest values in terms of Average Accuracy, Average Precision, and Average Recall for recognition. Specifically, the IATWD method attained an Average Accuracy of 95.19%, an Average Precision of 92.38%, and an Average Recall of 90.38%. Furthermore, as shown in Fig. 7, in a specific experiment, the recognition rates for the four classes of ships using the IATWD method were also the highest. Therefore, the IATWD method exhibits the most effective denoising and recognition performance for simulated ship signals.

5. Validation of IATWD Method Denoising through Experimental Data

5.1 Introduction to Experimental Data

Using a guidance head target detection platform, measurements were conducted on ships located on the surface of the Bohai Sea. This involved the collection of HRRPs from multiple angles for four different ships: the Weiqiao Jiada No. 16 (W-16, Fig. 8), Zhehai No. 169 (Z-169, Fig. 9), Yongxing Island (YXD, Fig. 10), and Bohaicuizhu (BHCZ, Fig. 11).

The study used experimental data comprising fifty sets per ship type, resulting in a total of two hundred sets of multi-angle high-resolution range profiles (HRRPs). These data sets were employed to validate the denoising method proposed in this study, which utilizes an improved wavelet threshold technique. Parameters of measured ships are shown in Tab. 8.

Target	Length	Width	Detection Distance
W-16	110 m	25 m	4900 m
Z-169	189.99 m	32.26 m	5300 m
YXD	167.25 m	25.2 m	5300 m
BHCZ	178.8 m	28 m	5100 m

Tab. 8. Target dimension parameters.

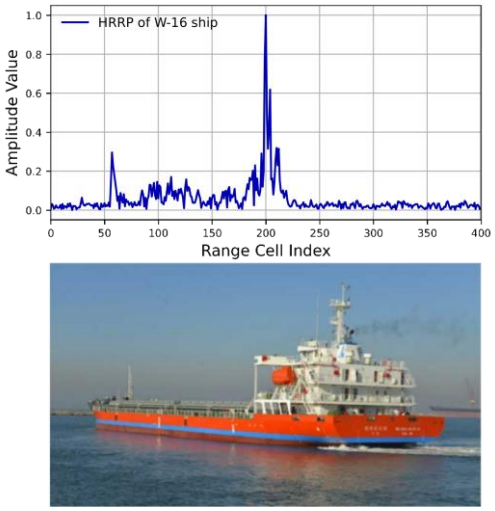

Fig. 8. HRRP and photograph of W-16 at an attitude angle of 64°.

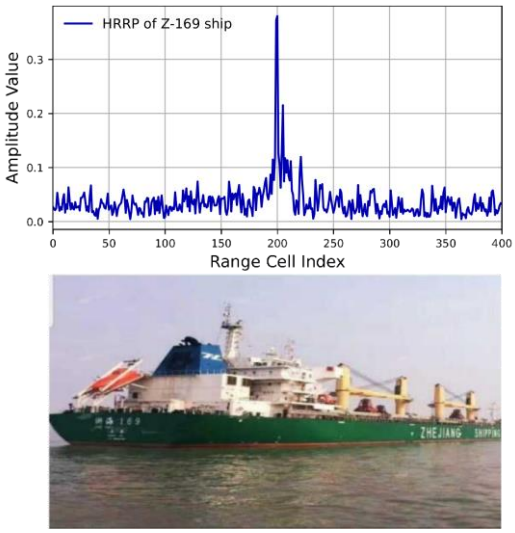

Fig. 9. HRRP and photograph of Z-169 at an attitude angle of 36°.

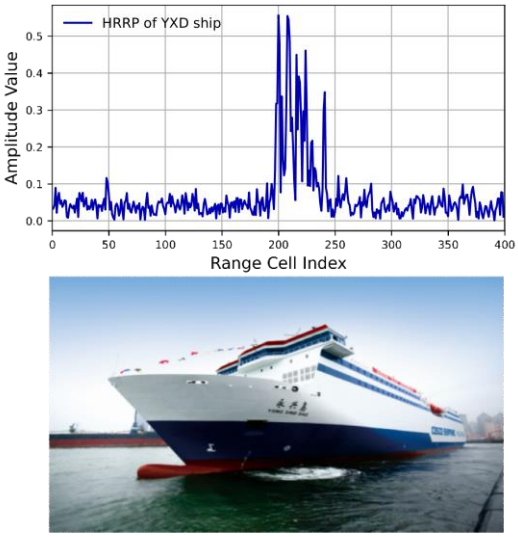

Fig. 10. HRRP and photograph of YXD at an attitude angle of 117°.

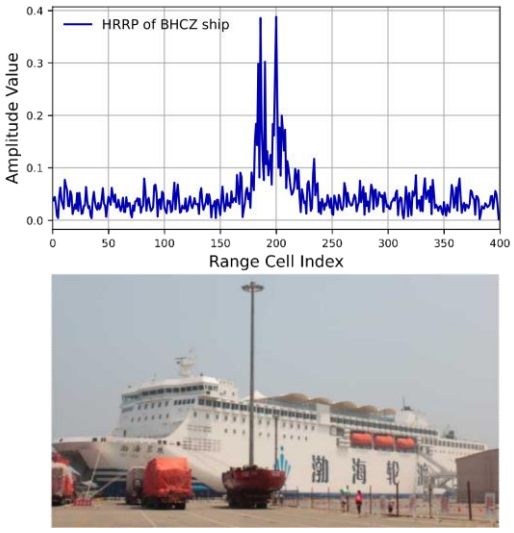

Fig. 11. HRRP and photograph of BHCZ at an attitude angle of 116°.

5.2 Analysis of Recognition Performance Using Empirical Data

The method employed for processing empirical data uses the same noise reduction parameters as those for simulated data, employing an SVM as the classifier. This involves using identical recognition parameters for target classification, and the effectiveness of various noise reduction techniques is evaluated by calculating their recognition rates. The test set for recognition consists of randomly selected 10 datasets from 50 datasets of four types of naval ships, with the remaining 40 datasets serving as the training set for recognition. This experiment was conducted ten times.

Due to the absence of original pure signals in the empirical data, it is not feasible to use indicators such as the SNR to determine the outcomes of noise reduction. Consequently, alternative methods must be employed to assess the effectiveness of the denoising algorithms. HRRP data has distinct peak characteristics that represent the real target signatures. The local peak signal-to-noise ratio (LPSNR) can effectively evaluate the performance of denoising algorithms in removing noise while preserving signal features. Additionally, the noise suppression effect can be assessed quantitatively by the energy ratio of the denoised and noisy signals. In this study, the total energy ratio and LPSNR metrics are employed to evaluate the denoising performance of different methods. The specific assessment metrics are as follows:

(1) Energy Ratio

$$\text{Energy Ratio} = \frac{E_{\text{total}}^{\text{denoised}}}{E_{\text{total}}^{\text{nosiy}}} = \frac{\sum |\hat{s}(n)|^2}{\sum |s(n)|^2}. \tag{28}$$

Here, $s(n)$ is the noisy signal, and $\hat{s}(n)$ is the corrected signal after denoising treatment.

(2) LPSNR

The formula for PSNR is as follows [33], [34]:

$$\mathrm{PSNR} = 20\log_{10}\left(\frac{L_{\max}}{\mathrm{RMSE}(s(n),\hat{s}(n))}\right). \quad (29)$$

Here, $L_{\max}$ is the peak amplitude of the signals, and RMSE($s(n)$, $\hat{s}(n)$) is the mean squared error between the corrected denoised signal and the noisy signal.

Analogous to the PSNR formula, the LPSNR for each local peak i in the noisy signal and the corrected denoised signal is:

$$\mathrm{LPSNR}_i = 20\log_{10}\left(\frac{|\hat{s}_i|}{\sigma_{\hat{s}_i}}\right) - 20\log_{10}\left(\frac{|s_i|}{\sigma_{s_i}}\right). \quad (30)$$

The average value of the LPSNR_i for all extracted local peaks, denoted as LPSNR, is as follows:

$$\mathrm{LPSNR} = \frac{1}{M}\sum_{i=1}^{M}\mathrm{LPSNR}_i. \quad (31)$$

Here, $|\hat{s}_i|$ is the amplitude of the the i-th local peak point of corrected denoised signal, $|s_i|$ is the amplitude of the i-th local peak point of noisy signal, $\sigma_{\hat{s}_i}$ and σ_{s_i} are the standard deviations of the background noise in the neighborhood around the peak point for the corrected denoised signal and noisy signal, $\sigma_{\hat{s}_i} = \mathrm{MAD}_{\hat{s}_i}/0.6745$, $\sigma_{\mathrm{ss}_i} = \mathrm{MAD}_{s_i}/0.6745$; M is the number of extracted local peaks.

The local peaks are extracted using the sliding window method, and a threshold is set to filter out small amplitude peaks. Suppose there is a signal $y = \{y_1, y_2, \ldots, y_n\}$, the set of local peaks P of this signal can be expressed as:

$$P = \{y_i \mid y_i > \max(y_{i-k/2},\ldots, y_{i+k/2}), y_i > T\}, \quad (32)$$

$$T = 0.625\times\frac{1}{N}\sum_{i=1}^{N} y_i. \quad (33)$$

Here, y_i is the i-th point in the signal; k is the size of the sliding window, and the range of the window is $[i-k//2, i+k//2]$, where k is an odd number; P is the set of local peaks, including all peak points that meet the above conditions; T is the threshold for the minimum amplitude, and only when y_i is greater than this threshold is it considered an effective local peak; N denotes the signal's length.

The total energy ratios and average LPSNR between noisy and corrected denoised data for all samples of empirical data are calculated. The results were presented in Tab. 9.

Figure 12 shows a comparative analysis of different denoising methods applied to a specific sample from the measured ship BHCZ. From Tab. 9 and Fig. 12, it is evident that the IATWD performs best. The Energy Ratio of this method is 0.8573, and the LPSNR is the highest at 3.64 dB. This indicates that the IATWD effectively removes noise and retains useful detail features.

Denoising Methods	Energy Ratio	Average LPSNR
Soft (visushrink)	0.6905	3.5
Hard (visushrink)	0.8742	3.53
Garrote (visushrink)	0.8139	3.55
IATWD	**0.8573**	**3.64**
Reference [16]	0.8926	0.45
Reference [17]	0.7746	2.33
Reference [18]	0.5951	–0.25

Tab. 9. Energy Ratio and Average LPSNR comparison of different signals.

In contrast, reference [18] performs the worst: its Energy Ratio is 0.5951, a large number of useful detailed features of the signal are lost, and less noise is removed, resulting in an extremely low LPSNR (only –0.25 dB).

Although the soft (visushrink) method has a relatively high LPSNR (3.5 dB), its Energy Ratio is very low, only 0.6905. This indicates that although this method removes the most noise, it over-smooths the signal, leading to excessive loss of the signal's detailed features. The Energy Ratios of garrote (visushrink) and reference [17] are 0.8139 and 0.7746, and the LPSNRs are 3.55 dB and 2.33 dB. Although these two methods remove a large amount of noise, the signals are still over-smooth, and the peak detail features are lost.

The Energy Ratio of the hard (visushrink) method is 0.8742, and the corresponding LPSNR is 3.53 dB. With this method, the peak features are effectively preserved, but there is residual noise, and the signal also has distortion and discontinuity problems. The Energy Ratio of reference [16] is 0.8926, and the LPSNR is 0.45 dB. Although the peak features are effectively preserved, there is more residual noise.

Consequently, the IATWD method designed in this study proves to be highly effective for empirical data, achieving the best denoising results.

Different Signal	Average Accuracy	Average Precision	Average Recall
Empirical data	86.88%	77.96%	73.75%
Soft (visushrink)	91.12%	83.49%	82.25%
Hard (visushrink)	90.25%	81.32%	80.5%
Garrote (visushrink)	91.75%	84.74%	83.5%
IATWD	**92.5%**	**87.03%**	**85%**
Reference [16]	89.89%	80.53%	79.75%
Reference [17]	90.87%	82.93%	81.75%
Reference [18]	88.75%	79.37%	77.5%

Tab. 10. Average recognition rates (%) for different measured signals.

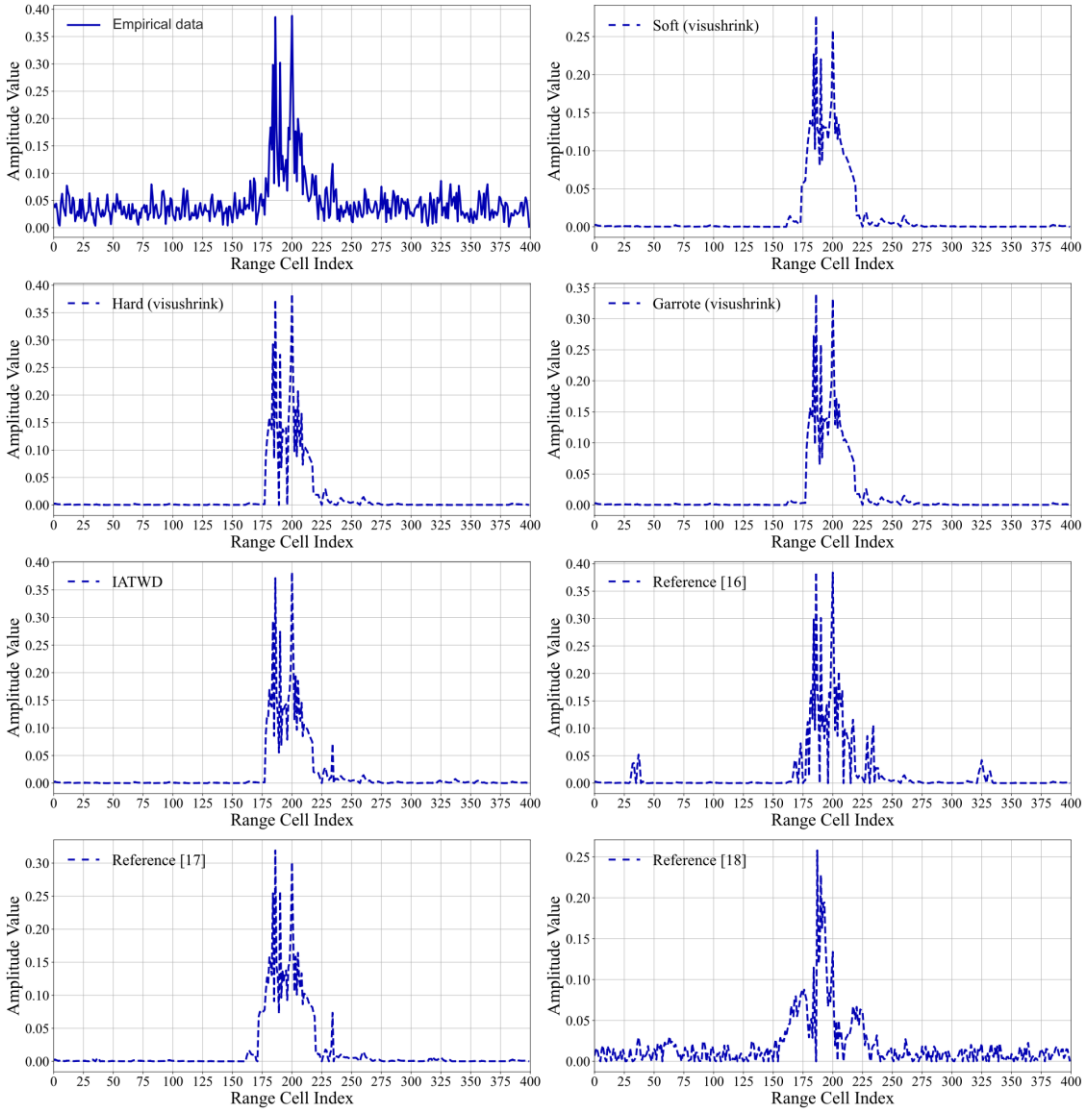

Fig. 12. Comparison of denoising methods for a sample from the measured ship BHCZ.

From Tab. 10 and Fig. 13, it can be inferred that the IATWD method, proposed in this study, achieves an average accuracy of 92.5%, an average precision of 87.03%, and an average recall of 85% for the measured naval ships. These metrics are the highest among the tested methods, indicating that the IATWD method effectively reduces noise interference in empirical data while preserving useful information, thereby enhancing target recognition performance.

6. Conclusion

To address the noise interference issues in actual one-dimensional range profile data from ships, this study utilized WD methods to preprocess the data. It proposed an improved TF based on an adaptive threshold with a variable factor, achieving better denoising results and enhancing target recognition performance. The key findings and contributions of this study are summarized as follows:

1. Considering the effects of decomposition scales, noise standard deviation per level, and signal length on threshold determination, an adaptive threshold formula was constructed. This was based on the conventional VisuShrink threshold but improved by combining the advantages of soft and hard TFs. The resulting function is continuous at thresholds T and kT, ensuring the smoothness of the denoised signal and reducing oscillations caused by denoising. It exhibits asymptotic behavior, which eliminates constant bias between the two approaches, thereby reducing signal loss after reconstruction. The introduction of a variable factor enhances the flexibility of using the TFs.

2. The noise of the HRRP signal exhibits DC bias characteristics. A one-dimensional minimum filtering estimation is used to correct the DC bias characteristics of the denoised signal, and the denoising effect analysis is performed on the corrected simulated data after denoising. Through the analysis of the interactions among wavelet base functions, decomposition levels, and the variable factor,

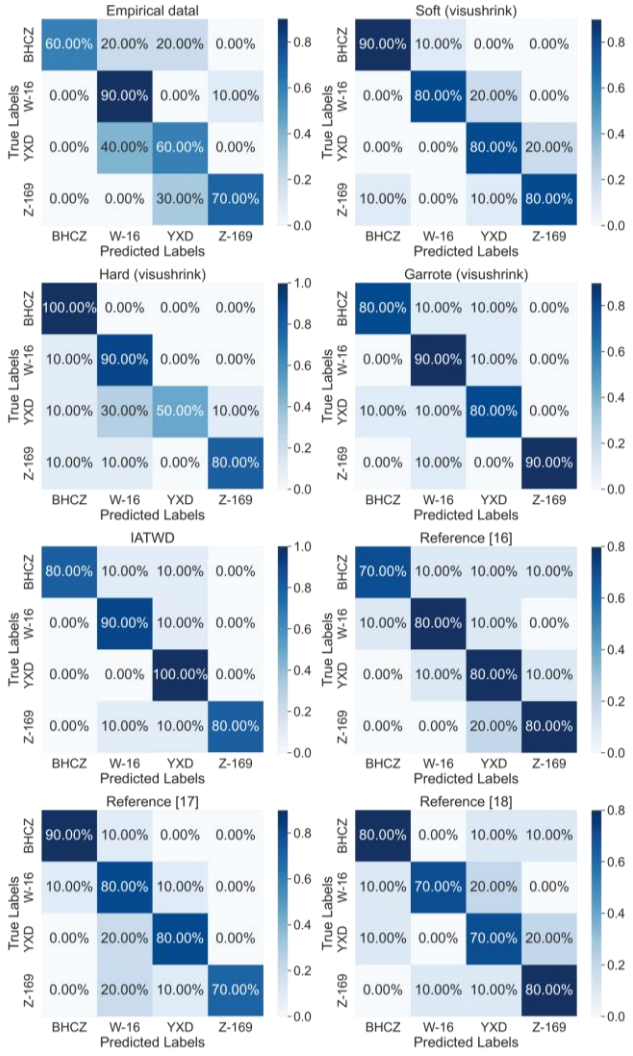

Fig. 13. Confusion matrix for the recognition of four types of measured ships.

optimal denoising parameters for the IATWD method were identified. Compared to other denoising methods, the IATWD method minimizes signal distortion and effectively preserves useful signal features. It achieves the highest average SNR and the lowest RMSE, indicating better denoising effectiveness. During recognition validation, it exhibited the highest average recognition rate among all denoising methods, with an average accuracy of 95.19%, an average precision of 92.38%, and an average recall of 90.38%, rendering it the most effective method in terms of recognition performance.

3. Given the absence of original pure signals in empirical data, traditional metrics such as SNR and RMSE have limited applicability. Therefore, Energy Ratio and LPSNR were proposed as alternative quantitative assessments. The results show that in the empirical data, the IATWD method achieves optimal performance in terms of Energy Ratio (0.8573) and LPSNR (3.64 dB), thereby balancing noise removal and the preservation of useful information; it also achieved the highest average recognition rate, with an average accuracy of 92.5%, an average precision of 87.03%, and an average recall of 85%. Thus, the IATWD method effectively mitigates noise interference and preserves useful information, thereby enhancing the recognition of empirical targets.

Future studies will focus on analyzing the HRRP data characteristics of measured naval ships. By integrating data characteristics with noise models, and combining WT with deep learning, this research aims to further improve both denoising effectiveness and recognition accuracy.

Acknowledgments

This research was funded by the Higher Education Innovation Fund Project of Gansu province, grant numbers 2023A-201.

Data Availability

The data that support the findings of this study are available from the corresponding author upon reasonable request.

Conflict of Interest Statement

The authors declare that they have no known competing financial interests or personal relationships that could have appeared to influence the work reported in this paper.

References

[1] WU, L., HU, S., XU, J., et al. Ship HRRP target recognition against decoy jamming based on CNN-BiLSTM-SE model. *IET Radar, Sonar and Navigation*, 2024, vol. 18, no. 2, p. 361–378. DOI: 10.1049/rsn2.12507

[2] ZHANG, L., HAN, C., WANG, Y., et al. Polarimetric HRRP recognition based on feature-guided Transformer model. *Electronics Letters*, 2021, vol. 57, no. 18, p. 705–707. DOI: 10.1049/ell2.12225

[3] AI, X., QIU, M., HU, Y., et al. Instantaneous length estimation of ships through wideband composite bistatic radar (in Chinese). *Journal of Electronics and Information Technology*, 2024, vol. 46, no. 3, p. 944–951. DOI: 10.11999/JEIT230088

[4] YANG, Y., YANG, B. Overview of radar detection methods for low altitude targets in marine environments. *Journal of Systems Engineering and Electronics*, 2024, vol. 35, no. 1, p. 1–13. DOI: 10.23919/JSEE.2024.000026

[5] LEE, P., THEOTOKATOS, G., BOULOUGOURIS, E. Robust decision-making for the reactive collision avoidance of autonomous ships against various perception sensor noise levels. *Journal of Marine Science and Engineering*, 2024, vol. 12, no. 4, p. 1–33. DOI: 10.3390/jmse12040557

[6] ZHANG, Q., SONG, C., YUAN, Y. Fault diagnosis of vehicle gearboxes based on adaptive wavelet threshold and LT-PCANGO-SVM. *Applied Sciences*, 2024, vol. 14, no. 3, p. 1–26. DOI: 10.3390/app14031212

[7] CHEN, Z. Signal recognition for English speech translation based on improved wavelet denoising method. *Advances in Mathematical Physics*, 2021, vol. 2021, no. 1, p. 1–9. DOI: 10.1155/2021/6811192

[8] ZHOU, Y., LI, J., YAN, H., et al. Low-frequency ultrasound thoracic signal processing based on MUSIC algorithm and EMD wavelet thresholding. *IEEE Access*, 2023, vol. 11, p. 73912 to 73921. DOI: 10.1109/ACCESS.2023.3296465

[9] HUSSAIN, N., HASANZADE, M., BREIBY, D., et al. Performance comparison of wavelet families for noise reduction and intensity thresholding in Fourier Ptychographic microscopy. *Optics Communications*, 2022, vol. 519, p. 1–10. DOI: 10.1016/j.optcom.2022.128400

[10] HE, C., SHI, H., SI, J., et al. Physics-informed interpretable wavelet weight initialization and balanced dynamic adaptive threshold for intelligent fault diagnosis of rolling bearings. *Journal of Manufacturing Systems*, 2023, vol. 70, p. 579–592. DOI: 10.1016/j.jmsy.2023.08.014

[11] MA, J., LI, H., TANG, B., et al. Rolling bearing fault diagnosis based on improved VMD-adaptive wavelet threshold joint noise reduction. *Advances in Mechanical Engineering*, 2022, vol. 14, no. 10, p. 1–16. DOI: 10.1177/16878132221128397

[12] GENG, Z., YUAN, K., MA, B., et al. Rolling bearing fault diagnosis based on ICEEMDAN-WTATD-DaSqueezeNet. In *2023 IEEE 12th Data Driven Control and Learning Systems Conference (DDCLS)*. Xiangtan (China), 2023, p. 1510–1515. DOI: 10.1109/DDCLS58216.2023.10166891

[13] ZHOU, X., KAN, Z., MENG, H., et al. Research on trenching data correction method based on wavelet denoising-Kalman filtering algorithm. *Arabian Journal for Science and Engineering*, 2023, vol. 48, no. 2, p. 1097–1117. DOI: 10.1007/s13369-022-06729-1

[14] SHENG, Z., TAO, M., YUE, L. Reduction of seismic random noise in mountainous metallic mines based on adaptive threshold RCSST (in Chinese). *Chinese Journal of Geophysics*, 2019, vol. 62, no. 10, p. 4020–4027. DOI: 10.6038/cjg2019M0441

[15] LIU, J., GU, Y., CHOU, Y., et al. Seismic random noise reduction using adaptive threshold combined scale and directional characteristics of shearlet transform. *IEEE Geoscience and Remote Sensing Letters*, 2019, vol. 17, no. 9, p. 1637–1641. DOI: 10.1109/LGRS.2019.2949806

[16] LI, L., LI, M., ZHANG, Q. Noise reduction algorithm of electric arc furnace sound signal based on CEEMDAN-improved wavelet threshold (in Chinese). *Journal of Qufu Normal University (Natural Science Edition)*, 2025, vol. 51, no. 1, p. 81–86. DOI: 10.3969/j.issn.1001-5337.2025.1.081

[17] LU, W., YE, C. L., ZHAO, C. Y., et al. Leakage identification for mineral air supply pipeline system based on joint noise reduction and ELM. *Measurement*, 2023, vol. 219, p. 1–18. DOI: 10.1016/j.measurement.2023.113304

[18] WU, F., MA, C., CHENG, K. Study on wavelet denoising method of vibration signal based on improved threshold (in Chinese). *Journal of Hefei University of Technology (Natural Science)*, 2022, vol. 45, p. 873–877. DOI: 10.3969/j.issn.1003-5060.2022.07.002

[19] HUANG, X., ZHANG, X., XIE, X., et al. Noise reduction and characteristic analysis of fluid signal in the jet impact-negative pressure deamination reactor based on wavelet transform. *Asia-Pacific Journal of Chemical Engineering*, 2024, vol. 19, no. 1, p. 1–15. DOI: 10.1002/apj.3001

[20] DAUBECHIES, I. *Ten Lectures on Wavelets*. PA (USA): Society for Industrial and Applied Mathematics, 1992. ISBN: 9780898712742. DOI: 10.1137/1.9781611970104

[21] BAI, J., CHEN, W., CAI, T. Compensation for MEMS gyroscope zero bias stability. In *2013 Chinese Automation Congress (CAC 2013)*. Changsha (China), 2013, p. 744–748. DOI: 10.1109/CAC.2013.6775833

[22] ZHU, J., FU, Z., LI, K., et al. Chromatography denoising with improved wavelet thresholding based on modified genetic particle swarm optimization. *Electronics*, 2023, vol. 12, no. 10, p. 1–18. DOI: 10.3390/electronics12204249

[23] KWON, J. H., NGUYEN, N. T., TRAN, M. T., et al. Robust detection of ductile fracture by acoustic emission data-driven unsupervised learning. *International Journal of Mechanical Sciences*, 2024, vol. 277, p. 1–19. DOI: 10.1016/j.ijmecsci.2024.109420

[24] HAN, G., XU, Z. Electrocardiogram signal denoising based on a new improved wavelet thresholding. *Review of Scientific Instruments*, 2016, vol. 87, no. 8, p. 084303-1–084303-6. DOI: 10.1063/1.4960411

[25] HOU, Y., QIAN, S. R., LI, X. M., et al. Application of vibration data mining and deep neural networks in bridge damage identification. *Electronics*, 2023, vol. 12, no. 17, p. 1–17. DOI: 10.3390/electronics12173613

[26] OUYANG, C., CAI, L., LIU B., et al. An improved wavelet threshold denoising approach for surface electromyography signal. *EURASIP Journal on Advances in Signal Processing*, 2023, vol. 108, no. 1, p. 1–24. DOI: 10.1186/s13634-023-01066-3

[27] SUN, Z., LU, J. An ultrasonic signal denoising method for EMU wheel trackside fault diagnosis system based on improved threshold function. *IEEE Access*, 2021, vol. 9, p. 96244–96256. DOI: 10.1109/ACCESS.2021.3093482

[28] HOU, J., LI, S., YANG, L., et al. Multi-leakage source localization of safety valve based on improved KDE algorithm. *Process Safety and Environmental Protection*, 2023, vol. 171, p. 493–506. DOI: 10.1016/j.psep.2023.01.027

[29] LIU, X., BIAN, S. F., DI, G. J., et al. The improved wavelet filtering algorithm based on Stein's unbiased risk estimation. *Science of Surveying and Mapping*, 2024, vol. 49, no. 12, p. 158 to 166. ISSN: 1009-2307

[30] HAO, Y. S., YE, Y. S., DENG, Z. M., et al. FEKO sparse micro-Doppler modeling and CS reconstruction method. *Editorial Office of Optics and Precision Engineering*, 2016, vol. 24, no. 6, p. 1482 to 1489. DOI: 10.3788/OPE.20162406.1482

[31] MALLAT, S. *A Wavelet Tour of Signal Processing: The Sparse Way*. 3rd ed. Florida (United States): Academic Press, Inc., 2008. DOI: 10.1016/B978-0-12-374370-1.X0001-8

[32] DU, L., HUA, H., LE, Z., et al. Noise robust radar HRRP target recognition based on scatterer matching algorithm. *IEEE Sensors Journal*, 2015, vol. 16, no. 6 p. 1743–1753. DOI: 10.1109/JSEN.2015.2501850

[33] MOORE, R., EZEKIEL, S., BLASCH, E. Denoising one-dimensional signals with curvelets and contourlets. In *2014 - IEEE National Aerospace and Electronics Conference (NAECON 2014)*. Dayton (OH, USA), 2014, p. 189–194. DOI: 10.1109/NAECON.2014.7045801

[34] GAO, Z., WANG, Y. Assessing 3D holographic reconstruction quality through the mean local peak signal-to-noise ratio metric. In *2024 5th International Conference on Computer Engineering and Application (ICCEA 2024)*. Hangzhou (China), 2024, p. 675–678. DOI: 10.1109/ICCEA62105.2024.10603571

About the Authors ...

Zirong HONG was born in 1986. He received his M.Sc. from Lanzhou Jiaotong University in 2014. Now he is a Ph.D. candidate in Lanzhou University of Technology.

His current research interest is target recognition and signal processing.

Qinfen LU was born in 1972. She is currently a Professor and Ph.D. Supervisor at the College of Electrical Engineering, Zhejiang University, China. Her research focuses on pattern recognition and motor drive control.

Guangqing BAO was born in 1972. She is currently a Professor and Ph.D. Supervisor at Southwest Petroleum University China. Her research focuses on pattern recognition and modern motor & motion control.